Energy Conversion and Management: X 30 (2026) 101499

Contents lists available at ScienceDirect

Energy Conversion and Management: X

journal homepage: www.sciencedirect.com/journal/energy-conversion-and-management-x

A simplified multi-physics approach for bifacial photovoltaic modules: Theory and validation of peculiar module layout

Emanuele Ogliari, Alberto Dolara, Domenico Mazzeo *, Luca Lazzari, Sonia Leva

Department of Energy, Politecnico di Milano, via Lambruschini, 8, 20156, Milano, Italy

ARTICLE INFO

Keywords:
Vertical bifacial photovoltaics
View factor method
Optical–electrical–thermal modeling
Ground albedo
Parameter identification
Particle filter

ABSTRACT

This work aims to develop and integrate three sub-models into a simplified multi-physics tool for simulating bifacial PV (bPV) devices. While similar tools exist, they often rely on complex modeling. In contrast, this study investigates a simpler approach that achieves comparable accuracy. The proposed models are also experimentally validated under a specific case study: a Vertical Bifacial PV (VBPV) installation. This setup is relatively novel and provides valuable insights into the feasibility of VBPV systems for agricultural and space-constrained applications, highlighting the strong dependence between environmental conditions and PV module performance.

For the optical model, a 2D View Factor method is implemented, demonstrating high sensitivity to the module's surroundings. Results show that this simplified approach can achieve errors below 5%. The electrical modeling is the core of this study. Two parameter estimation methods are applied: a traditional experimental data-fitting approach and a data-driven stochastic method based on Particle Filtering. The latter is an innovative technique for this type of estimation. Three different electrical models for bPV are numerically solved and compared, showing good accuracy, with errors below 4%. Notably, a newly proposed circuit model outperforms the other two. A simplified 0-D lumped thermal model is developed and validated to complete the multi-physics framework, showing deviations of up to 7% in temperature estimation.

The integration of the best-performing electrical model with the optical and thermal sub-models results in a comprehensive tool capable of estimating power and energy with errors of 5% and 2%, respectively. These findings demonstrate that a simplified approach could support the estimation of PV performance based on field measurements and weather data for VBPV installations.

1. Introduction

Accurate modeling of photovoltaic (PV) systems is essential to evaluate the overall benefits of PV installations in terms of energy yield, reduction of carbon emissions, and payback time. Emerging technologies, such as bifacial PV (bPV) modules, introduce new complexities that require specific modeling approaches. The advantages of bPV technology are well-established, including lower levelized costs of electricity [1,2] and improved performance compared to monofacial PV (mPV) systems [3]. However, the accurate modeling of bPV generators in outdoor conditions remains an ongoing issue.

The primary challenge lies in accurately calculating the global solar irradiance on the bPV module face not affected by direct irradiance. Two main approaches suitable to address this issue are: the View Factor (VF) method and the ray tracing method. The VF method, while less accurate, is more straightforward to implement and has been extensively studied [4,5]. In contrast, ray tracing offers higher precision, but it comes with the drawbacks of increased computational complexity and simulation time, limiting its widespread application [6,7].

The second important problem is the electrical modeling of bPV systems, which requires representing all electrical effects related to the incident solar irradiance on both sides of the bPV cells. Early studies suggested modeling the electrical output as a superposition of front (the side with the higher conversion rate) and rear (the side where the junction box is placed) contributions [8]. However, most researchers have adopted an approach based on the IEC 60904-1-2 standard [9], where the bPV module is treated similarly to an mPV system exposed to an equivalent irradiance represented as the weighted sum of front and rear in-plane irradiance. Studies comparing bPV models demonstrate that various approaches can achieve good agreement with experimental data but often necessitate more intensive development [10]. Despite recent proposals, empirical models are data-fitting tools that do not capture the governing physics, limiting their

* Corresponding author.
E-mail address: domenico.mazzeo@polimi.it (D. Mazzeo).

https://doi.org/10.1016/j.ecmx.2025.101499
Received 22 July 2025; Received in revised form 24 October 2025; Accepted 24 December 2025
Available online 26 December 2025

transferability [11]. Additionally, beyond the electrical model itself, the procedure for determining the parameters involved is not well-defined and requires further investigation. Finally, their thermal behavior is more complex due to non-uniform heat distribution caused by variable rear-side illumination and albedo effects [12]. Several thermal models have been developed to predict the operating temperature of bPV modules, ranging from empirical correlations to detailed heat transfer modeling. Empirical models, such as the modified Nominal Operating Cell Temperature (NOCT) model and Sandia model, often oversimplify heat transfer mechanisms, leading to inaccuracies under varying environmental conditions. More advanced approaches, such as physical models, provide higher accuracy by resolving radiative and convective cooling effects. Nevertheless, most existing models lack seamless integration with optical and electrical models, which is critical for holistic bPV performance prediction. A key research gap remains in developing a user-friendly yet accurate thermal model that efficiently couples with optical and electrical sub-models while accounting for bifacial-specific thermal effects. Such a model should reduce computational overhead without sacrificing precision, enabling broader adoption in PV system design and energy yield forecasting. These coupled gaps, namely, the need for a lightweight yet integrated optical–electrical–thermal treatment under rear-side illumination and albedo-driven non-uniformities, motivate our focus on Vertical Bifacial PV Systems (VBPVs) and frame the objectives detailed below.

In this context, this research focuses on VBPVs because their installation conditions accentuate exactly the phenomena highlighted above (rear-side irradiance, albedo sensitivity, and non-uniform thermal behavior), thus providing a stringent testbed for an integrated yet simplified multi-physics approach. Beyond their scientific interest, VBPVs are also gaining traction in land-constrained and agrivoltaic settings, where vertical layouts can mitigate land-use competition while exploiting seasonally varying diffuse and reflected components for energy production [13–15].

Accordingly, this study aims to develop and validate a simplified multi-physics tool for predicting bPV output power—integrating optical, electrical, and thermal sub-models—with a specific focus on VBPVs installations, in which optical, electrical, and thermal couplings are most pronounced, thereby creating a coherent bridge to the study objectives.

While similar tools exist, such as the one proposed by Gu et al. [16] or the one from commercial software such as PVsyst [17] or SAM [18], this work presents a comparative analysis of two optical models, three electrical models, and a thermal simplified model, addressing gaps in the literature and advancing limited research in modeling this technology. In particular, from the optical point of view, the novel based on the albedo variable model is developed and validated. Additionally, from the electrical point of view, this paper presents an innovative electrical equivalent model for the bPV technology. Besides, the Particle Filter (PF) algorithm for estimating electrical parameters is presented here, enhancing the accuracy and robustness of the model. Finally, an extensive experimental validation of the proposed multiphysics model was performed over 12 days, showing different seasonal and weather features.

This paper is organized as follows: Section 2 details the development of a multi-physics model for bPV systems, integrating optical, electrical, and thermal sub-models. A 2D View Factor method estimates front and rear in-plane irradiance, while two established electrical models and a newly proposed one compute the module's electrical output. A 0-D lumped thermal model accounts for temperature effects. The model is validated using real-world data from a VBPV installation described in Section 3. Independent validation, results, and comparisons with experimental data are presented in Section 4, with key conclusions and future developments discussed in Section 5.

2. Proposed models

This contribution targets a compact formulation that integrates measurements and enables fast simulations for screening and control, emphasizing an adequate accuracy/cost trade-off. The bPV multi-physics model consists of three interacting sub-models for optical, electrical, and thermal simulation. A schematic overview of the complete model is presented in Fig. 1.

As illustrated in Fig. 1, the optical sub-model takes the Global Horizontal Irradiance (GHI) and the Diffuse Horizontal Irradiance (DHI) as data input and generates as outputs the global irradiance on the two sides of the bPV module, which in turn are part of the set of inputs for the electrical and thermal models, together with the air temperature. The output of the multi-physics model is the bPV module's I–V curve, from which the maximum power output is calculated.

For the optical and electrical sub-models, different modeling criteria have been evaluated. The optical sub-model is based on a 2-D approach, and both the constant albedo and the variable albedo scenarios have been assessed. The electrical sub-model is based on the most suitable of three equivalent circuits. Finally, the thermal model is based on a 0-D energy balance.

2.1. Optical models

Two optical models have been analyzed in the following subsections. The nomenclature for the electrical models is reported in (see Table 1).

2.1.1. Optical model – OPT1

The proposed optical model uses meteorological data, system geometry, and ground reflectivity to compute the total irradiance on the module surfaces. It is a simplified version of the well-known View Factor (VF) method commonly found in heat transfer textbooks in [19] and applied in the bPV field in [4,5,16]. The model considers a single, infinitely long row of PV modules and adopts the following simplifying assumptions: a two-dimensional geometric projection with a 2-D view-factor formulation; Lambertian (isotropic) reflection from the illuminated ground; isotropic diffuse sky irradiance; a ground surface that is purely reflective (non-emitting); and a negligible contribution of sky-reflected radiation on the illuminated ground. The ground surface is divided into three portions: two are directly illuminated (g_1) and (g_3), and the other, which is shadowed by the module (g_2), as shown in Fig. 2. For each portion, a view factor coefficient for both the front (f) and rear (r) surfaces of the module is computed, given the geometrical configuration.

The in-plane irradiance components are calculated starting from the global horizontal irradiance, GHI, diffuse horizontal irradiance, DHI, and direct normal irradiance, DNI., As shown in Eq. (1), direct irradiance, G_{dir}, is obtained from basic theory on sun position over a generic fixed surface, tilted of the angle β, oriented with the azimuth α, using the incidence angle, θ_s, and zenith angle θ_z, with n_s being the orthogonal direction on the surface [20]. Fig. 3 shows how the different angles are involved in the system.

Diffuse irradiance on front and rear surfaces (G_{dif}) is calculated from sky view factors (Fv_{sky}) as shown in Eq. (2). Finally, the irradiance on the front and rear surfaces that is reflected off the ground (G_{ref}) is calculated for each ith portion of the ground, as in Eq. (3) as the product of the global irradiance incident on the ground by the ground albedo (ϱ) and the corresponding view factor (Fv_{g_i}) between the ith portion of the ground and the receiving surface (front or rear). To determine view factors, a 2-D projection using Hottel's crossed-string method [21] determines the relationship between radiation reaching a given surface and that emitted from another.

$$G_{dir,s} = \begin{cases} DNI \cdot \cos(\theta_s), & \text{if } -90° \le \theta_s \le +90°, \\ 0, & \text{otherwise} \end{cases} \quad (1)$$

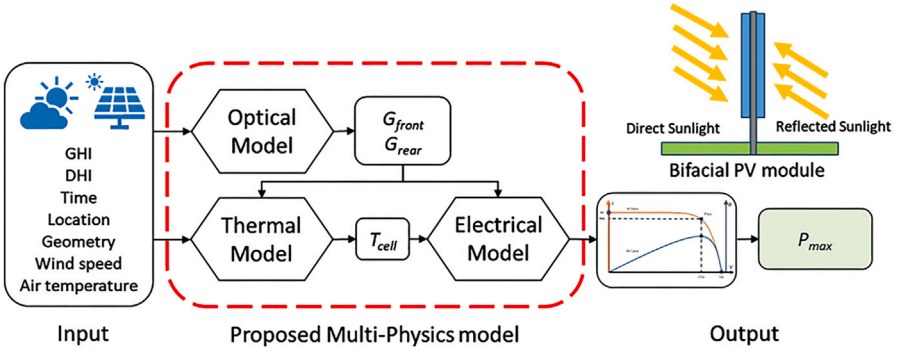

Fig. 1. Model flow diagram.

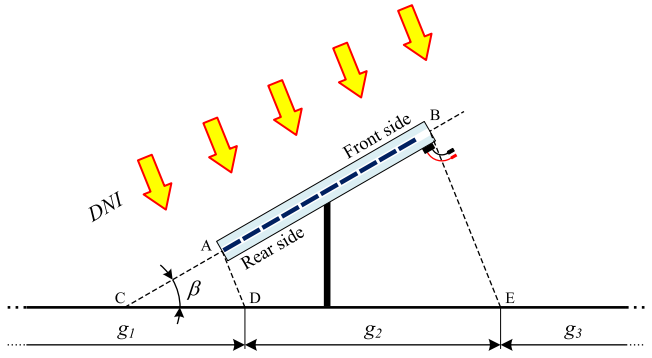

Fig. 2. Coordinate system representing the simulated setup.

Table 1
Optical models parameters.

Symbol	Name	Unit
GHI	Global Horizontal Irradiance	W/m^2
DHI	Diffuse Horizontal Irradiance	W/m^2
DNI	Direct Normal Irradiance	W/m^2
G_{dir}	In-plane direct irradiance	W/m^2
G_{dif}	In-plane diffuse irradiance	W/m^2
G_{ref}	In-plane reflected irradiance	W/m^2
β	Tilt angle	rad
θ_z	zenith angle	rad
θ_s	Surface incidence angle	rad
α	Surface azimuth angle	rad
Fv	View factor coefficient	–
ϱ	Albedo	–
R_r	Reflected radiation ratio	–

$$G_{dif,s} = DHI \cdot Fv_{sky,s} \tag{2}$$

$$G_{ref,s,g_i} = GHI \cdot \varrho \cdot Fv_{s,g_i} = (DNI \cdot cos(\theta_Z) + DHI) \cdot \varrho \cdot Fv_{s,g_i} \tag{3}$$

where the subscript s indicates the side of the module: $s = f$ stands for front side and $s = r$ stands for rear side. It is worth noting that, in Eq. (1), $\theta_r = \theta_f + 180°$. Front and rear irradiance components are:

$$G_f = G_{dir,f} + G_{dif,f} + \sum_{i=1}^{3} G_{ref,f,g_i} \tag{4}$$

$$G_r = G_{dir,r} + G_{dif,r} + \sum_{i=1}^{3} G_{ref,r,g_i} \tag{5}$$

For g_1 and g_3 ground portions, the diffuse irradiance in Eq. (3) is considered negligible due to the ground properties, namely $DHI = 0$ for the ground reflected irradiance calculation, both on front and rear surfaces. In this work, both scenarios with constant and variable albedo have been considered.

2.1.2. Optical model – OPT2

The second optical model is based on the *Type 16* from the Transient System Simulation Tool (TRNSYS18) [22,23]. Like OPT1, OPT2 takes GHI and DHI as inputs and computes in-plane components at each time step. The sun's position in the sky is determined similarly to the previous model, leading to similar results in direct irradiance. The diffuse irradiance is instead calculated based on the Perez model [24]. This model accounts for circumsolar, horizon brightening, and isotropic diffuse radiation by empirically derived "reduced brightness coefficients".

The contribution of reflected irradiance on a tilted surface is calculated by assuming the ground acts as an isotropic reflector and defining R_r as the ratio of reflected irradiance on a tilted surface to the total irradiance on a horizontal surface as:

$$R_r = 0.5 \cdot (1 - cos(\beta)) \cdot \varrho \tag{6}$$

$$G_{ref} = GHI \cdot R_r \tag{7}$$

Also in this model, the albedo can be treated as either constant or variable during the simulation.

The total irradiance on the surface is given by the contribution of direct, diffuse, and reflected radiation.

2.2. Electrical models

Conventional electrical modeling approaches for simulating the behavior of mPV devices are primarily based on the single-diode and double-diode models. For bPV modules, these models are extended to account for rear-side irradiance effects, which contribute additional photocurrent generation and influence both the thermal and electrical operating conditions. In the literature, two main approaches are commonly used to model bPV modules, resulting in different circuit topologies, both derived from the one-diode equivalent model. One of them represents the bifacial cell as a parallel connection of two mPV cells, each representing the contributions of front and rear irradiance, respectively; the parameters of each sub-model are therefore determined through mPV tests, in which one side of the module is exposed to irradiance while the other side is covered with a non-reflective black-cover. The other modeling approach introduces an additional current source into the conventional mPV cell model to account for the photogenerated current due to the rear-side irradiance; the parameters of the passive elements within the equivalent circuit—such as series and shunt resistances, as well as diode characteristics—are then calibrated to represent the electrical behavior of a bPV module.

In this work, three distinct electrical models have been defined and compared to identify the best-performing equivalent circuit; a summary

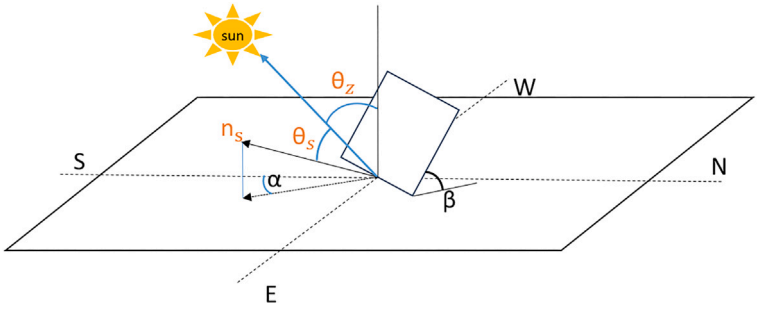

Fig. 3. Angles of radiation for a generic tilted surface.

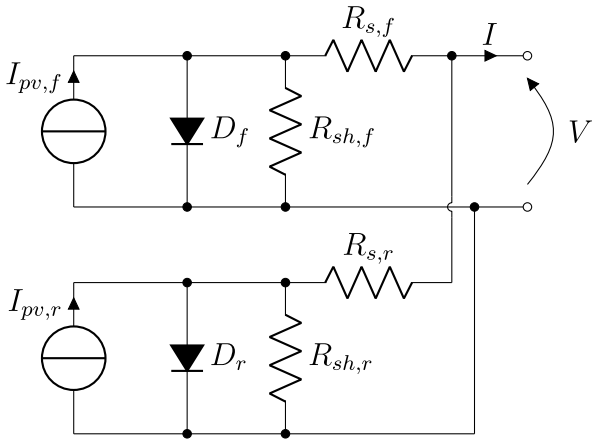

Fig. 4. Parallel model equivalent circuit.

Table 2
List of the electrical model parameters.

Symbol	Name	Unit
$I_{pv,f}$	Front photo-generated current	A
$I_{pv,r}$	Rear photo-generated current	A
$I_{pv,bi}$	Bifacial photo-generated current	A
$I_{0,f}$	Front reverse saturation current	A
$I_{0,r}$	Rear reverse saturation current	A
$I_{0,bi}$	Bifacial reverse saturation current	A
$R_{s,f}$	Front series resistance	Ω
$R_{s,r}$	Rear series resistance	Ω
$R_{s,bi}$	Bifacial series resistance	Ω
$R_{sh,f}$	Front shunt resistance	Ω
$R_{sh,r}$	Rear shunt resistance	Ω
$R_{sh,bi}$	Bifacial shunt resistance	Ω
n_f	Front diode ideality factor	–
n_r	Rear diode ideality factor	–
n_{bi}	Bifacial diode ideality factor	–

of these approaches is provided in the following paragraphs. The list of parameters of each equivalent circuit is presented in Table 2.

2.2.1. Electrical model – EL1

The first model, hereinafter referred to as EL1 or as the Parallel Model, represents the bPV cells as two mPV cells, one for the front and one for the rear side, connected in parallel. The resulting equivalent circuit is represented in Fig. 4. This modeling approach, which represents the bifacial module as two mPV cells connected in parallel, is widely reported in the literature [25] and is also used in various simulation software packages [26]. Although this model exhibits lower performance compared to other approaches [27], it is still investigated both to assess its accuracy and for its ease of characterization, as it inherits all the well-established procedures used for mPV modules. Indeed, the Parallel Model requires independent characterization of the front and rear surfaces to extract two distinct sets of five parameters. The equation that relates the voltage and current at the terminals of the bPV module is:

$$I = I_{\mathrm{pv,f}} - I_{0,f}\left(e^{\frac{V+I\cdot R_{s,f}}{n_f V_t}} - 1\right) - \frac{V + I\cdot R_{s,f}}{R_{sh,f}} + \\ + \left(I_{pv,r} - I_{0,r}\left(e^{\frac{V+I\cdot R_{s,r}}{n_r V_t}} - 1\right) - \frac{V + I\cdot R_{s,r}}{R_{sh,r}}\right) \tag{8}$$

2.2.2. Electrical model – EL2

The second model, hereinafter referred to as EL2, is a new proposal in the field of bPV modeling. This approach extends the modeling criterion for mPV cells under partial shading [28] to bPV cells, accounting for irradiance mismatch caused by the unequal illumination of the front and rear faces. Unlike the EL1 model, which treats the two faces as separate PV cells connected in parallel, this proposed modeling framework considers the physical configuration of the bPV cell, characterized by a single PN junction and, therefore, a single junction voltage. The resulting equivalent circuit is represented in Fig. 5, together with its simplified version arising from the parallel equivalents of circuit elements.

The resulting model can be classified as a dual-diode configuration, and the equation that relates the voltage and current at the terminals of the bPV module is:

$$I = I_{pv} - I_{0,f}\left(e^{\frac{V+I\cdot R_{s,f}}{n_f V_t}} - 1\right) - I_{0,r}\left(e^{\frac{V+I\cdot R_{s,r}}{n_r V_t}} - 1\right) - \frac{V + I\cdot R_s}{R_{sh}} \tag{9}$$

where the series resistance (R_s), the shunt resistance (R_{sh}) and photo-generated current (I_{pv}) are:

$$R_s = \frac{R_{s,f}\cdot R_{s,r}}{R_{s,f} + R_{s,r}} \tag{10}$$

$$R_{sh} = \frac{R_{sh,f}\cdot R_{sh,r}}{R_{sh,f} + R_{sh,r}} \tag{11}$$

$$I_{pv} = I_{pv,f} + I_{pv,r} \tag{12}$$

The EL2 equivalent circuit can also be obtained from the EL1 equivalent circuit by introducing a short-circuit connection between the anode of the diodes included in the front and rear face equivalent circuits, thereby setting a single voltage across the PN junction within the bPV cell. This circuit-theory-based approach outlines how to correlate the EL2 model parameters with those of the EL1 model. Although several methods exist in the literature to derive double-diode model parameters from the front and rear cell models [25,29], in this work, the EL2 parameters are obtained by combining those of the EL1 model as in (10), (11), and (12).

2.2.3. Electrical model – EL3

The third model, hereinafter referred to as EL3, uses the single-diode model, representing the bPV module as an equivalent mPV module.

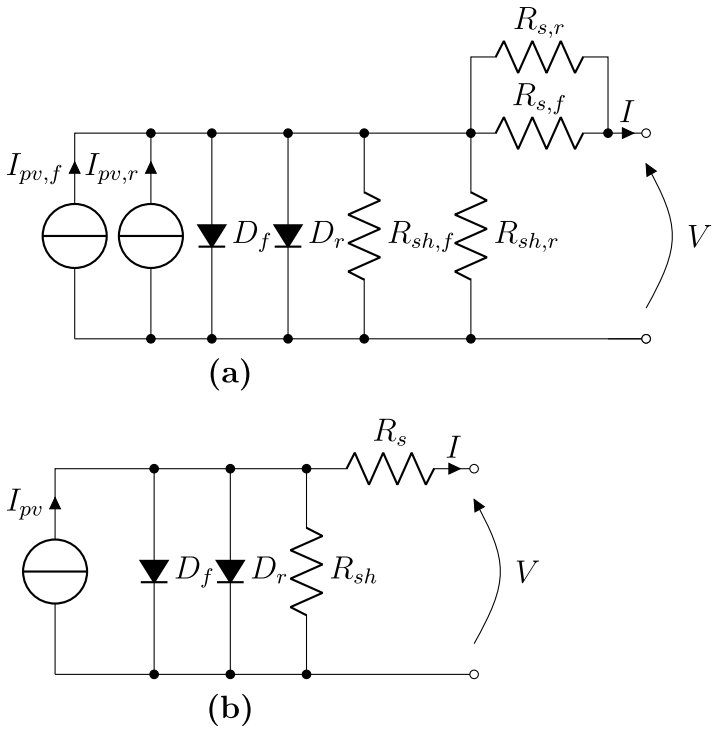

Fig. 5. Equivalent circuit EL2: (a) equivalent circuit derived from the modeling criterion and (b) 2-diode equivalent circuit after substituting the series and parallel equivalents of resistances and the current sources.

This approach is specified in the IEC 60904-1-2 standard [9], is widely adopted in the literature, and is generally considered the most accurate. To account for the irradiance on both sides of a bPV module, this approach defines an equivalent irradiance as the weighted sum of the front and rear irradiance; the weighting reflects the different conversion efficiencies of the two surfaces. The equivalent irradiance is calculated using Eq. (13) where the Bifaciality Factor (BI) is the ratio of the rear-side efficiency to the front-side efficiency, measured under Standard Test Conditions (STC).

$$G_{eq} = G_f + BI \cdot G_r \tag{13}$$

The equation that relates the voltage and current at the terminals of the bPV module is:

$$I = I_{pv} - I_0 \cdot \left(e^{\frac{V+R_s \cdot I}{n \cdot V_t}} - 1 \right) - \frac{V + R_s \cdot I}{R_{sh}} \tag{14}$$

The equivalent circuit is the one shown in Fig. 6, and requires only five parameters. For a mPV module, the model parameters are calculated under STCs, whereas for a bPV module, there is no well-defined irradiance configuration for parameter extraction; the standard IEC 60904-1-2 references only the equivalent circuit, and in the literature, only a few approaches are currently available, typically based on combinations of parameters related to mPV operation [25,27].

2.2.4. Parameter estimation and their variation with temperature and irradiance

The different parameters of the electrical models have been estimated by using two methods: Fitting and PF. Furthermore, some comments on the influence of environmental conditions are included.

Parameter estimation – Fitting. The circuit model parameters can be determined using two main approaches [30]: by leveraging datasheet values through the solution of appropriate nonlinear systems, or by fitting experimental data. In this work, the latter approach, based on experimental data, is adopted. For the electrical model EL1—and consequently EL2, which uses parameter combinations derived from EL1—curve fitting, is applied to the equation Eq. (14) to identify the set of parameters that best fits the experimental I–V curves of the front and rear surfaces under mPV operating conditions. A nonlinear least-squares fitting method is applied. Then, the specific parameters of each test are adjusted to represent the operation in STC using Eqs. (19)–(21).

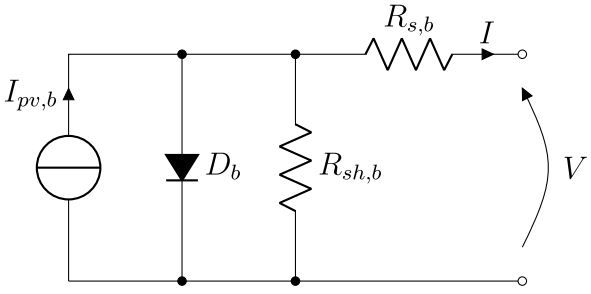

Fig. 6. Bifacial model equivalent circuit.

Parameter estimation – Particle filter. The PF approach has been proposed in [31] for mPV modules. In this work, the PF has been extended to a bifacial module and applied to EL3 only. Unlike the Fitting method, which can be applied to a few measurements, the PF approach needs to be conducted on a dataset with measurements from the entire experimental campaign. This method is based on Sequential Monte Carlo simulation [32], where parameter estimation is achieved by assigning likelihood weights to each of the p possible parameter sets (also called particles). These weights, obtained by comparing the model's power output with the experimental data, refine the parameter estimation. The problem needs to be discretized into k steps, and a Monte Carlo scheme numerically approximates the parameters. An initial state is assumed and iteratively updated based on the previous parameter estimation to enhance convergence.

$$\phi_{k,i} = \phi_{k-1,i} + \epsilon_{k-1,i} \quad i = 1, \ldots, p \tag{15}$$

The non-linear model, in this case the electrical model, is described by $\mathbb{G}$ and depends on the set of five parameters ϕ and on the environmental conditions b. The model is also characterized by the noise presented by ζ.

$$P_{max,k} = \mathbb{G}(\phi_k, b_k, \zeta_k) \tag{16}$$

By calculating the modeled power and comparing it with the experimental value, it is possible to obtain a weight, ω, for each of the particles based on a Gaussian likelihood distribution, $\mathcal{L}$.

$$\omega_{k,i} = \frac{\mathcal{L}_{k,i}}{\sum_{i=1}^{p} \mathcal{L}_{k,i}} \tag{17}$$

Finally, for each step, the estimation of the most probable state is calculated by the sum of each particle solution multiplied by its weight. The process is repeated for the next step.

$$\phi_k = \sum_{i=1}^{p} \omega_{k,i} \cdot \phi_{k,i} \tag{18}$$

Irradiance and temperature influence on equivalent-circuit parameters. For all models, the parameters used in the equivalent circuits need to be corrected to account for actual operative conditions in terms of front and rear irradiances, as well as cell temperature T_c. In the electrical model, the cell temperature is denoted T_c. We couple the electrical and thermal models by setting $T_c = T_{\mathrm{pv}}$. This choice follows the lumped assumption, whereby T_{pv} is representative of the module (and thus of the cell). STCs are chosen as a reference considering the mPV operation with a front side irradiance of 1000 W/m^2 and a cell temperature of 25 °C. Since PV modules generally operate under non-standard conditions, it is necessary to include in the PV cell electrical model the dependence of its parameters on both irradiance and PV cell temperature. The literature presents different approaches—sometimes exhibiting opposite trends—regarding the dependence of equivalent circuit parameters on temperature and irradiance [33]. Furthermore, different sets of electric model parameters might lead to very similar I–V curves [34], making the most accurate set of equations for correcting the parameters with respect to irradiance and temperature dependent on the method used to extract them at STC.

Among the available sets of equations for adjusting the PV cell electrical model parameters with respect to both irradiance and cell temperature, the following set has been applied to all the electrical models used in this work:

$$I_{pv} = I_{pv,ref} \cdot \frac{G}{G_{ref}} \cdot \left(1 + \alpha_{pv} \cdot \left(T_c - T_{c,ref}\right)\right) \tag{19}$$

$$I_0 = I_{0,ref} \cdot \left(\frac{T_c}{T_{c,ref}}\right)^3 \cdot e^{\left(\frac{E_g}{n \cdot k \cdot T_{c,ref}} \cdot \left(1 - \frac{T_c}{T_{c,ref}}\right)\right)} \tag{20}$$

$$R_{sh} = R_{sh,ref} \cdot \frac{G_{ref}}{G} \tag{21}$$

$$R_s = R_{s,ref} \tag{22}$$

$$n = n_{ref} \tag{23}$$

Previous studies [30] have already shown that this set of equations generates accurate results when applied together with the STC parameter extraction methods used in this work.

2.3. Thermal model – TH

The thermal balance of a bPV includes the simultaneous presence of longwave and shortwave radiative heat exchanges and convective heat exchanges between the external environment and both rear and front surfaces of the bPV module. In addition, the heat introduced from both bPV module sides is transferred by heat conduction through the module. In the approach proposed, a detailed modeling of the surface heat exchanges between each surface and the environment is applied, and to maintain model simplicity, a 0-D lumped thermal model is developed for the heat conduction, assuming negligible temperature variation through the module's thickness, with cell and surface temperatures considered equal. The nomenclature for the thermal model is reported in Table 3. Modeling of convective and radiative heat transfer processes is adapted from the mPV model in [35]. The thermal balance model is reported in Eq. (24):

$$\Delta \dot{E}_n = \dot{E}_{in} - \dot{E}_{out} \tag{24}$$

The thermal power entering the system $\dot{E}_{in}$ is the solar irradiance on both sides of the bPV module, while the thermal power leaving the system $\dot{E}_{out}$ is the convective and radiative heat exchanges due to the interaction with the environment. The difference between these contributions results in the time derivative of the thermal energy stored inside the bPV module, $\Delta \dot{E}_n$, which is dependent on the bPV module's equivalent thermal capacity, C_T, due to the contribution of each layer. The front and rear surface properties, as well as the air temperature and wind velocity, are used to calculate convective and radiative heat transfer coefficients, h_{con} and h_{rad}, respectively. The explicit form of the thermal balance is:

$$\begin{aligned}\frac{C_T}{\Delta t}\left(T_{pv}(t-1) - T_{pv}(t)\right) = {} & A_{pv}\left((\tau\alpha)_f G_f + (\tau\alpha)_r G_r\right) \\ & - A_{pv}\Big[h_{rad,sky,f}(T_{pv} - T_{sky}) + h_{rad,sky,r}(T_{pv} - T_{sky}) \\ & + h_{rad,g,f}(T_{pv} - T_g) + h_{rad,g,r}(T_{pv} - T_g) \\ & + h_{con,f}(T_{pv} - T_a) + h_{con,r}(T_{pv} - T_a)\Big] - P_{\max}.\end{aligned} \tag{25}$$

In Eq. (25), T_{pv} denotes the PV temperature representative of the module/glass-cover/lumped temperature of the 0-D thermal model. In the previous electrical modeling, the cell temperature is denoted T_c and is assumed equal to T_{pv} ($T_c = T_{\mathrm{pv}}$), consistent with the lumped assumption that T_{pv} represents the entire module. In general, T_c is experimentally measurable (e.g., surface thermocouples on the glass cover or IR thermography); however, within the 0-D formulation, it is the unknown lumped state obtained by solving the energy balance in Eq. (25). In addition, t is the time, A_{pv} is the module surface and $(\tau\alpha)$ is the factor that represents the surface's optical properties. The convective heat transfer coefficient is calculated by the superposition of natural and forced convection, given the wind speed and air temperature [36]. The radiative heat transfer coefficient is computed using Eq. (26) linearization of the longwave radiative heat exchanges and, consequently, simplifying thermal balance (ϵ is the surface emissivity, σ the Stefan–Boltzmann constant).

$$h_{rad} = Fv \cdot \sigma \cdot \epsilon \cdot (T_{pv}^2 + T_b^2) \cdot (T_{pv} + T_b) \tag{26}$$

T_{sky} is the sky temperature, T_g is the ground temperature. The sky temperature is determined by the Swinbank equation [37]. The ground surface temperature is equal to the air temperature. The electrical power $P_{\max}$ generated by the bPV module is neglected since the module is not in operation during the case study. While optical–electrical-1D thermal (O–E–T) models (e.g., Gu et al. [16]) can resolve through-thickness gradients and certain dynamic effects, a direct, like-for-like comparison requires a dedicated 1-D implementation with harmonized inputs and parameters, which is not yet available from the authors and will be developed in follow-up work.

3. Experimental setup

The experimental setup is based on a 345 W bPV module mounted on a dedicated structure designed to avoid partial shading on both surfaces of the bPV module.

The module involved in this experimental campaign is the 3S DUAL 72N by Enel Green Power 3SUN®, of which the electrical characteristics

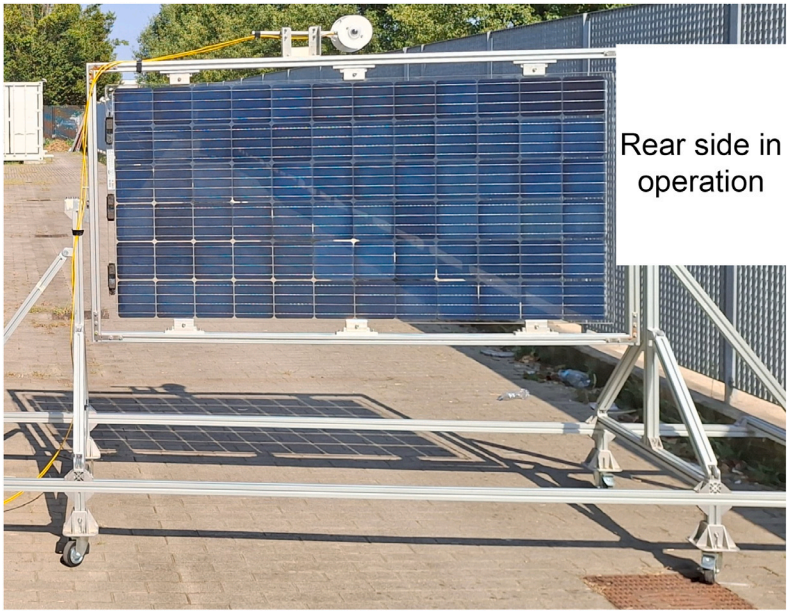

Fig. 7. Vertical setup of the module.

Table 3
Thermal model parameters.

Symbol	Name	Unit
E_n	Energy	Wh
C_T	Thermal capacity	J/(m^2 K)
t	Time	s
T_c	Cell temperature	K
T_{pv}	Photovoltaic temperature	K
T_a	Air temperature	K
T_{sky}	Sky temperature	K
T_g	Ground temperature	K
h_{con}	Convective heat transfer coefficient	W/(m^2 K)
h_{rad}	Radiative heat transfer coefficient	W/(m^2 K)
$(\tau\alpha)$	Transmission factor	–
σ	Stefan–Boltzmann constant	W/(m^{2}K^4)
ϵ	Emissivity	–
Fv	View factor coefficient	–
A_{pv}	Photovoltaic area	m^2

Table 4
3S DUAL 72N bifacial module—STC data.

Modules Parameters and specifications		
Module type	3SBA345A	
Maximum power	P_{max}	345 W
Voltage at maximum power	V_{mpp}	39.30 V
Current at maximum power	I_{mpp}	8.78 A
Open-Circuit voltage	V_{oc}	47.90 V
Short-Circuit current	I_{sc}	9.18 A
Module efficiency	η	17.4%
Bifaciality factor	BI	85.7%
I_{sc} temperature coeff.	α_{pv}	0.048%/° C

are listed in Table 4. The module is mounted vertically (tilt angle β = 90°). The front face looks East; the module azimuth α = −90° (relative to South) as presented in Fig. 7. This setup simulates the basic element of a bPV generator in the agricultural PV application.

A total of 12 days are collected throughout a year, including different seasonal (i.e., Spring and Summer) and weather conditions: cloudy, variable, and sunny. The environmental parameters, such as the irradiance components, wind speed, and air temperature, are collected using $SolarTech^{LAB}$ [38] weather station, while the PV module-specific parameters such as cell temperature, output power, and in-plane front and rear irradiance are measured using HT® I-V500w and HT® Solar02 with a Resistance Temperature Detector (RTD). Two reference cells as specific to the location, solar radiation sensors are installed on the PV module frame as shown in Fig. 7. Measurements and devices are summarized in Table 5.

Table 5
Metrological characteristics of measuring instruments.

Device	Parameter	Symbol	Accuracy
HT I-V500w Solar02	Max DC Power	P_{max}	±1%
	Cell Temperature	T_c	±1%
	Front irradiance	G_f	±3%
	Rear irradiance	G_r	±3%
Weather station	Global irradiance	GHI	±0.1%
	Diffuse irradiance	DHI	±0.1%
	Air Temperature	T_a	±0.1%
	Wind speed	u_{wind}	±0.1%

3.1. Electrical circuit parameters and models validation procedures

The parameter estimation has been performed with the bPV module in vertical position, facing south, and parameters have been calculated in different time frames with similar weather conditions, as much as possible closer to the STC ones. The whole procedure follows the accuracy requirements and a preliminary set-up of the instrument of measurement, in compliancy with the IEC 60904-1-2 standard [9] as summarized in Table 6.

In addition, for the OPT, EL, TH, and Multi-physics models validation, the experimental activity followed the steps listed below:

1. Check instrumentation, according to the requirements shown in Table 6
2. Positioning of bPV module in east–west orientation (azimuth = −90°)
3. I–V curve weather parameters recording every 5 min
4. Inversion of albedometer at noon (rotated vertically by 180°)
5. Deployment of model under validation to simulate the quantity of interest (i.e., MPP)

Table 6
Experimental data recording and checks summary compliant with IEC 60904-1-2.

Experimental Requirements and Checks	
Sensors	• I–V: uncertainty at V_{OC}, I_{SC} < 0.2% • Temperature: uncertainty < 1°C • Irradiance (RD): Pyranometer
Setup	TD–RD co-planarity: ±2°
C1: Irradiance Components and Uniformity	(Subscripts: d=diffuse, r=rear-side, f=front-side) ✓ $G_{d,f} < 0.3G_f$ ✓ $G_r < 3\,W/m^2$ ✓ $G = G_{ref} \pm 20\%$
C2: Irradiance Stability	✓ $\frac{\Delta G}{G(t_0)} = \frac{G(t_N) - G(t_0)}{G(t_0)} < 1\%$
C3: Reporting/Post-processing	✓ $T_{RD}(I_{sc})$ differs > 2°C from calibration ✓ $T_{RD}(P_{max})$ differs > 0.5°C ✓ T_{TD} differs > 1°C from reported T ✓ G differs > 0.5% from reported G ✓ Spectral response difference (RD–TD)
Notation	• T: junction temperature • TD: test device (DUT) • RD: reference device (irradiance sensor)

6. Calculation of the error metrics between the model estimation and the actual parameter value

4. Model validation and results

The data collected during the experimental campaign consisted of input and output data for the specific sub-models, allowing their independent validation to evaluate the accuracy of each sub-model. The proposed 0-D thermo–electrical workflow is validated experimentally using measurement campaigns, including synchronized module-surface temperatures and electrical outputs under varied irradiance, wind, and ambient conditions; metrics are reported against the measured variables.

Regarding the optical models, the comparison between the proposed VF factor model (OPT1) and the TRNSYS model (OPT2) supports the close dependence between optical model sensitivity and environmental factors. Furthermore, the validation of the electrical model is required to address the most suitable model among the three presented.

The validation process is mainly based on the Root Mean Square Error (RMSE). It is calculated by taking the square root of the squared differences between the observed values (y) and the predicted values ($\hat{y}$) divided by the number of samples (m). In addition, the normalized RMSE is calculated by dividing the previously calculated RMSE by the maximum value in the interval (y_{max}):

$$RMSE = \sqrt{\frac{\sum (y - \hat{y})^2}{m}} \tag{27}$$

$$nRMSE = \frac{RMSE}{y_{max}} \tag{28}$$

Secondly, R^2 is used; it is based on a statistical approach and indicates the size of the simulated residuals compared to those of a null model where all predictions are equal to the mean value. High R^2 values are preferable, with the two extreme values of 0 and 1 indicating the worst and perfect models, respectively.

$$R^2 = 1 - \frac{\sum (y - \hat{y})^2}{\sum (y - \bar{y})^2} \tag{29}$$

To better understand the accuracy of the model, the error is defined as in Eq. (30) to quantify the deviation of simulated data from the expected value. Moreover, the relative error ε_r is calculated following Equation (31).

$$\varepsilon = \hat{y} - y \tag{30}$$

Table 7
Optical models accuracy comparison on the whole period of analysis.

Error	Constant ρ				Variable ρ			
	OPT1		OPT2		OPT1		OPT2	
	Front	Rear	Front	Rear	Front	Rear	Front	Rear
$RMSE$ [W/m^2]	51.4	81.6	67.6	66.0	28.8	60.3	61.8	51.3
$nRMSE$ [%]	7.5%	11.0%	9.8%	8.9%	4.2%	8.1%	8.9%	6.9%
R^2 [–]	0.939	0.887	0.881	0.856	0.966	0.907	0.928	0.901

$$\varepsilon_r = \frac{\hat{y} - y}{y} \tag{31}$$

Additionally, the results from the multi-physics model are also analyzed with the Mean Absolute Error (MAE) and Mean Bias Error (MBE). They are described by Eqs. (32) and (33).

$$MAE = \frac{1}{m} \cdot \sum |\hat{y} - y| \tag{32}$$

$$MBE = \frac{1}{m} \cdot \sum (\hat{y} - y) \tag{33}$$

4.1. Optical model validation

Fig. 8 shows the front and rear in-plane irradiance on July 29, 2024; the experimental data and model results, computed with Eqs. (1)–(7), are compared. This day is chosen as an example, and identical analyzes were developed for all other days of the experimental campaigns. The figure shows that both optical models can follow the specific irradiance on the site with low divergence from the real irradiance. Table 7 shows a quantitative comparison between the two optical models for the whole period of analysis. The TRNSYS model (OPT2) is more consistent between the front and rear sides, while the model developed in this work (OPT1) is less accurate on the rear side.

A qualitative comparison across different days reveals that sunny days, such as July 29, 2024, or April 11, 2025, which are dominated by direct irradiance, exhibit higher accuracy ($nRMSE = 6\%$). In contrast, cloudy and variable days, such as July 8, 2024, result in greater deviations ($nRMSE = 21\%$). This increased deviation can be attributed to the dominance of diffuse irradiance, where lower measurement values amplify relative errors. Furthermore, site-specific factors, such as reflections from nearby buildings or objects, can alter the irradiance reflected to the module. These observations suggest a strong correlation between site conditions and model performance.

All previous results from the optical models were obtained by fixing the value of albedo, ρ, to 0.1. Given the high deviation, the scenario with a variable albedo is taken into consideration. The magnitude of albedo for each sample is calculated by rewriting Eqs. (4) and (5) starting from experimental data. The obtained value is clamped between 0 and 1 to obtain physical solutions. Fig. 9 reports the comparison of the two models with the experimental data using a variable albedo. The numbers in Table 7 confirm, for both models, the improvement using a variable albedo.

4.2. Electrical models validation

The validation of electrical models involves two parts: the first consists of validating the parameters of the circuit elements that constitute them, and then the circuits themselves with the aim of identifying the best one.

The validation of the parameters is carried out with reference to a single day by comparing a few key points of the measured and calculated IV characteristics.

The maximum power points, normalized over the maximum values, of all the I–V curves calculated with the two parameter estimation procedures (Fitting and PF) are plotted against the recorded ones in

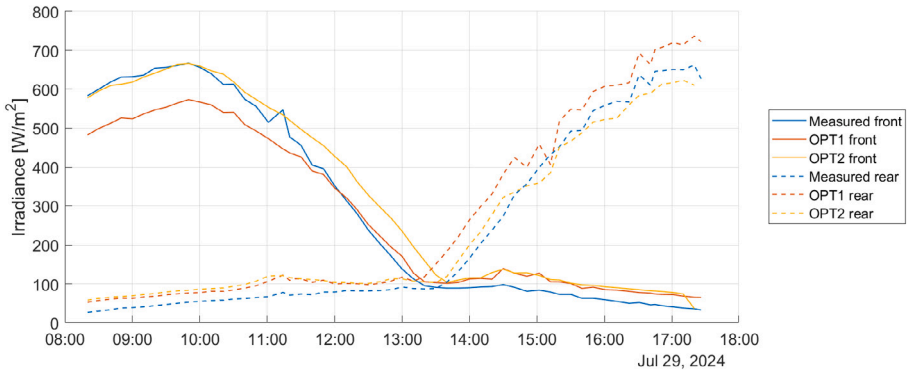

Fig. 8. Front and rear in-plane irradiance collected on July 29, 2024, considering a constant albedo.

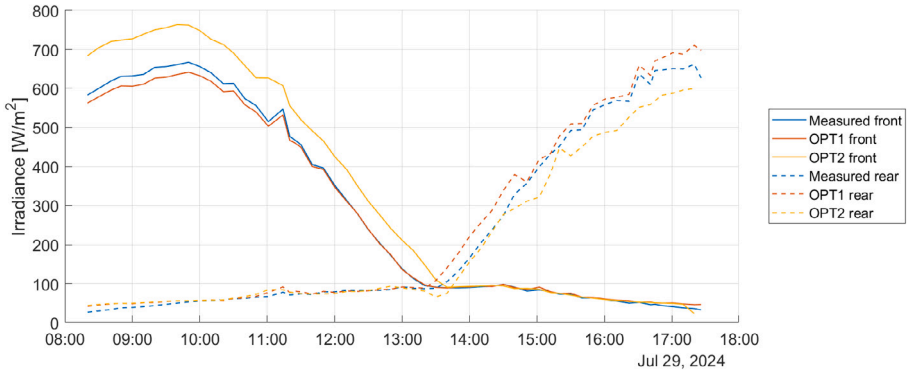

Fig. 9. Front and rear in-plane irradiance collected on July 29, 2024, considering a variable albedo.

Fig. 10 on July 29, 2024. The graph on the left demonstrates that all three electrical equivalent models (EL1, EL2, and EL3) show excellent agreement with experimental measurements, with data points clustering tightly around the bisector line within a ±10% tolerance band. This suggests that parameter estimation through the fit function is robust across different model architectures for standard operating conditions. The right graph focuses specifically on the bifacial model EL3 with parameters derived from a PF approach, showing similarly strong correlation, but with a slightly wider ±15% tolerance band. The comparable performance between Fitting methods validates the reliability of both parameter estimation techniques, though the fit function approach appears to yield marginally tighter predictions across the model ensemble.

Here, among the different values of the I–V curves, only the Maximum Power Points are shown as they are the quantity of main interest for most applications and also because a large number of instruments process this important data.

The second step compares EL1, EL2, and EL3 to identify the best-performing model in terms of power and energy accuracy. To do so, both power and energy estimation accuracy are compared to the experimental values.

The power curve, obtained by the models on July 29, 2024, is shown in Fig. 11. It highlights that each model performs similarly overall, with certain regions where one model aligns more closely with experimental data and others where deviations appear. Considering the error metrics of power for the whole period in Table 8, the EL1 and EL2 are the ones that perform better with a value of R^2 of 0.996 compared to 0.990 for the Bifacial models (EL3), while EL2 is only slightly better in RMSE/nRMSE.

Evaluating the energy estimation capability of the models, the EL2 better approximates the measured 11.77 kWh with a value of 11.65 kWh. The Parallel model (EL1) underestimates the output with 11.63 kWh, while the Bifacial model (EL3) overestimates the energy with a production of 12.31 kWh.

Table 8
Comparison of the electrical models. Power accuracy evaluated in the whole period of the experimental campaign.

Error	EL1	EL2	EL3
$RMSE$ [W]	5.60	5.59	9.08
$nRMSE$ [%]	2.44%	2.43%	3.95%
R^2 [-]	0.996	0.996	0.990

Performing a qualitative comparison with environmental factors for each day of measurements, the models are less responsive on cloudy days and tend to diverge more from the real power curve. In contrast, on sunny days, the correspondence is much better. This observation can have two main reasons: the quality of measurements on cloudy days, where weather stability can affect the collected data, and the other is related to some hypotheses that neglect mismatch effects between cells in the module.

4.3. Thermal model validation

The temperature estimation was also performed on July 29, 2024 by the thermal model (TH). The TH estimation accuracy shows an $nRMSE$ of 6.93%. Possible temperature deviations are due to the simplifications made in the TH model and to environmental-specific characteristics. This simplified thermal model allows for gross estimation of the temperature, which is used by the multi-physics approach, aiming at providing the electrical power output of the bPV module.

4.4. Multi-physics model

The proposed Multi-physics model is made of the best, independently validated optical and electrical models, namely OPT1, EL2.

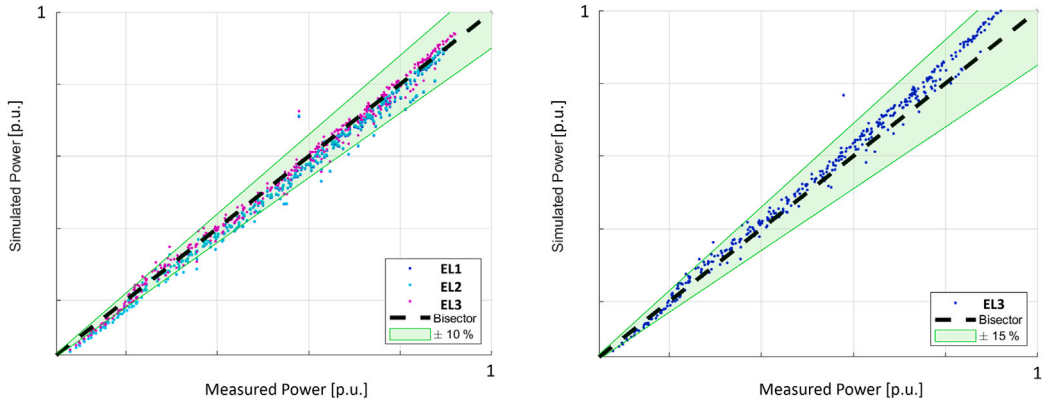

Fig. 10. Electrical model validation and comparison. Left: Three models with parameters from the fit function. Right: Bifacial model with parameters from Particle Filter.

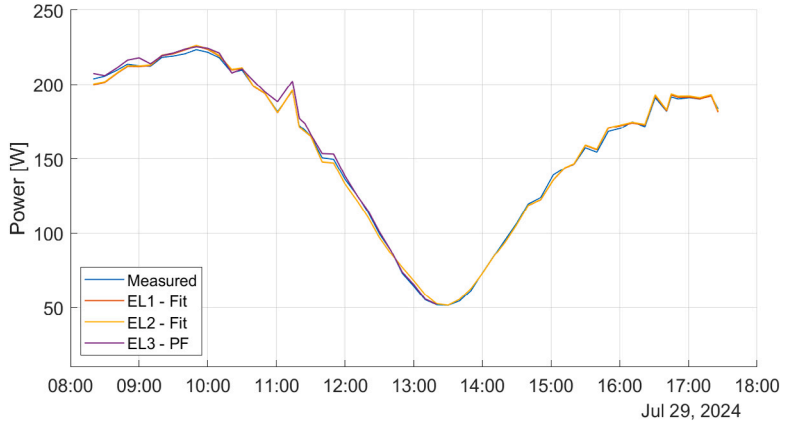

Fig. 11. Power curves obtained by using the different electrical models on July 29, 2024.

The thermal model TH has been added as well. The proposed Multi-physics model is evaluated on different days. For completeness, both the constant albedo and variable albedo scenarios are considered.

Figs. 12 and 13 show the power curve obtained on July 29, 2024, and on April 11, 2025, respectively. Both days are sunny: July 29, 2024, represents summer conditions, while April 11, 2025, represents spring conditions with lower air temperature. It is possible to see that for the scenario with constant albedo, the orange curve, the $nRMSE$ result is about 10.67% and $R^2 = 0.834$ for July 29, 2024, and the $nRMSE$ result is about 8.23% and $R^2 = 0.901$ for April 11, 2025. When considering the albedo variable, the yellow curve, the power estimation results in an $nRMSE$ of 4.27% with R^2 equal to 0.973 on July 29, 2024, and in an $nRMSE$ of 4.97% with R^2 equal to 0.938 on April 11, 2025.

The energy estimation from the model resulted in 1.48 kWh and 1.36 kWh considering constant albedo, and 1.44 kWh and 1.33 kWh for the scenario with variable albedo.

Table 9 shows the error trend in terms of power of all the periods of the measurement campaign when considering the multi-physics model in the scenario with a variable albedo. In addition, the columns with daily mean air temperature ($\bar{T}_a$), the daily mean global horizontal solar irradiance ($G\bar{H}I$), and the relative error on the daily energy (ε_r) are included. The most remarkable result is that, on the whole period, the $nRMSE$ is 8.6% with an R^2 of 0.932, showing a good performance of the proposed multi-physics approach in the chosen bPV layout.

According to Table 9, there is not a consistent linear relationship between mean daily temperature and $nRMSE$: high mean air temperature values can correspond to both high and low $nRMSE$. Daily mean GHI appears to have a weak inverse relationship with $nRMSE$: in general, higher GHI tends to correspond to lower $nRMSE$, possibly due to more stable solar irradiance patterns on sunny days. However, $nRMSE$ is likely influenced by multiple interacting factors, not just GHI or air temperature alone. The mean error $\overline{nRMSE}$ of power calculated for each typology of daily weather is reported in Table 10.

Therefore, it can be inferred that Sunny days have the lowest average $nRMSE$, indicating better model performance under stable, predictable solar conditions. Cloudy and variable weather yield higher $nRMSE$, likely due to irregular irradiance patterns and increased model uncertainty. This shows a clear correlation between weather typology and $nRMSE$—the more stable the weather, the lower the $nRMSE$.

Additionally, the error distribution of the multi-physics model with constant and variable albedo over the entire period is shown in Fig. 14. The multi-physics model demonstrates significant improvement when albedo correction is applied. This is well highlighted by the shape of the two error distributions: Fig. 14(b) (variable albedo) shows a narrower, more peaked error distribution than Fig. 14(a).

This adjustment accounts for site-specific characteristics and indirectly addresses factors neglected in the simplified optical model (OPT1).

5. Concluding remarks and future outlook

The research conducted in this study validates a new simplified multi-physics approach for modeling bPV modules through an experimental campaign with a Vertical Bifacial PV (VBPV) installation. The proposed optical model (OPT1), despite site-specific sensitivity

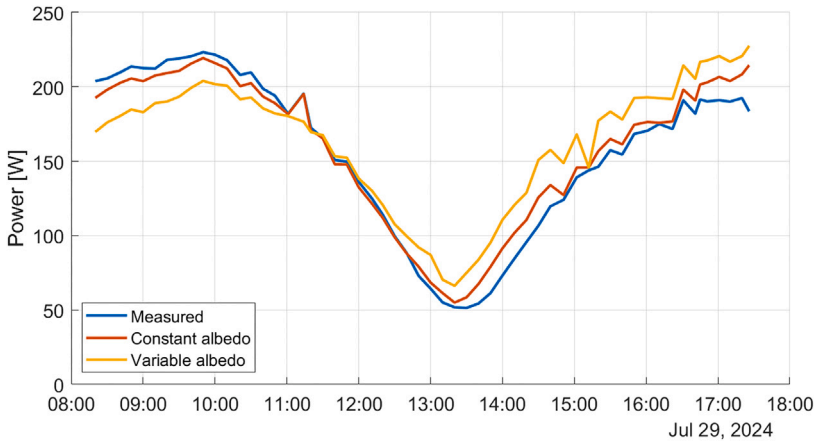

Fig. 12. Power curve of the multi-physics model (OPT1 + EL2 + TH) on July 29, 2024.

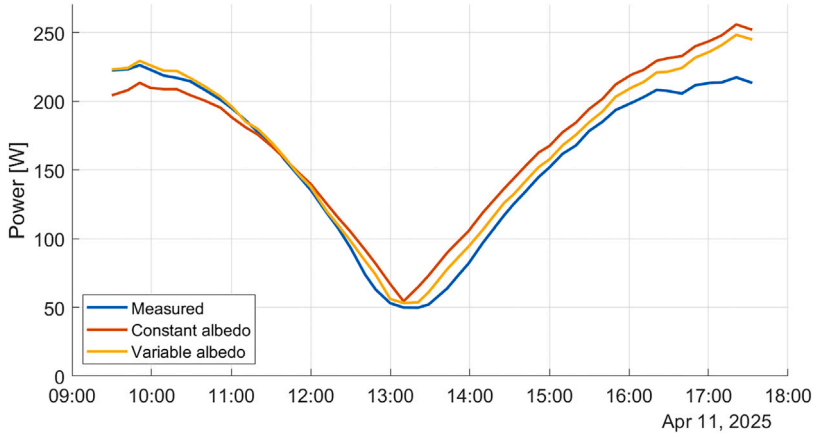

Fig. 13. Power curve of the multi-physics model (OPT1 + EL2 + TH) on April 11, 2025.

Table 9
Error metrics on different days considering a variable albedo.

Daily Features				Power			Energy
Date	Weather type	$\bar{T}_a$ [° C]	$G\bar{H}I$ [W/m^2]	*RMSE* [W]	*nRMSE* [%]	R^2 [–]	ϵ_r [%]
08/07/2024	Cloudy	25.23	272.7	27.42	13.92	0.789	24.5
09/07/2024	Sunny	27.49	283.77	21.69	9.80	0.843	10.8
25/07/2024	Variable	30.34	401.49	20.61	9.41	0.870	12.1
26/07/2024	Variable	28.94	289.27	19.13	8.90	0.882	13.5
29/07/2024	Sunny	29.57	306.86	9.54	4.27	0.973	1.8
31/07/2024	Variable	29.8	336.51	16.67	10.01	0.807	11.7
01/08/2024	Cloudy	29.52	255.92	13.07	6.65	0.942	1.7
02/08/2024	Sunny	28.51	285.44	13.35	5.81	0.960	2.6
10/04/2025	Sunny	15.41	261.6	11.25	5.76	0.964	5.2
11/04/2025	Sunny	16.22	269.51	13.27	4.97	0.938	4.9
29/04/2025	Sunny	20.51	299.38	28.59	13.82	0.693	12.4
15/05/2025	Sunny	21.08	331.65	27.06	12.16	0.785	14.5
Total	–	–	–	19.80	8.60	0.932	8.7

Table 10
Average nRMSE of power by weather typology.

Weather type	Days count	$\overline{nRMSE}$ [%]
Sunny	8	7.92%
Variable	3	9.44%
Cloudy	2	10.29%

and errors ranging from 4% to nearly 11% under variable conditions, achieves realistic estimations suitable for preliminary assessments. The models were implemented in MATLAB/Simulink® for reproducible I–V and MPP computations.

Comparisons among the three electrical models reveal that the Bifacial model (EL3), based on IEC 60904, exhibits lower accuracy. This outcome is likely due to the chosen parameter estimation approach, which is less robust and not yet well-established as an alternative method. In contrast, EL2 (dual-diode, single-junction) and EL1 (Parallel) models demonstrate better suitability for modeling bPV, achieving power and energy errors below 3% and 2%, respectively.

Electrical models that use parameters from the Fitting approach show the highest accuracy, with the best-performing model (EL2)

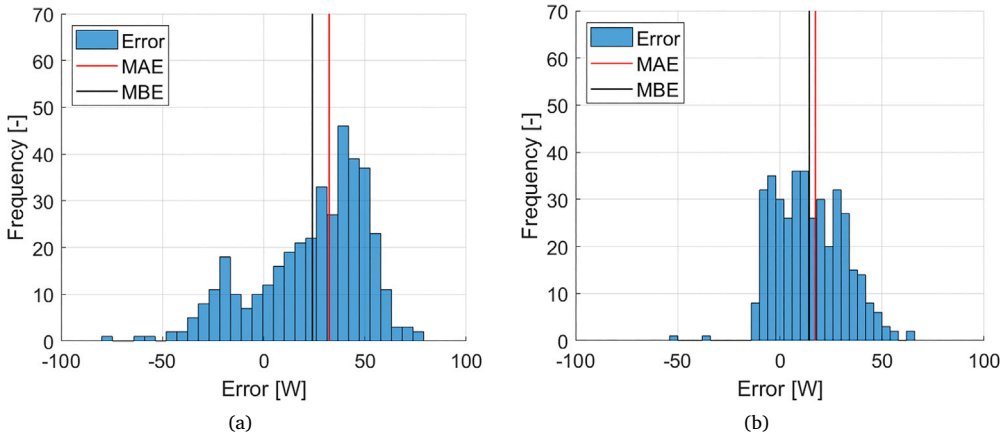

Fig. 14. Multi-physics model error (ε) distribution, MAE and MBE in the scenarios with constant (a) and variable (b) albedo.

achieving an almost zero energy deviation, 11.65 kWh modeled versus 11.77 kWh measured, resulting in a relative error of only −1.03% over the entire campaign. The well-known parallel model (EL1) follows closely, while the third model (EL3), which employs the PF algorithm for parameter estimation, is slightly less accurate but simpler to implement. Overall, all models demonstrate high accuracy, with R^2 values close to unity, indicating minimal differences in performance. However, further investigation is needed to refine parameter estimation methodologies and assess their impact on model accuracy.

The thermal model (TH) shows a 93% accuracy in cell temperature calculation. Like the optical model, it suffers from the environmental influence of the sites and simplification assumptions.

The multi-physics model resulting from the coupling of the optical model (OPT1), thermal model (TH), and Series electrical model (EL2) achieves power estimations within a 14% deviation when considering constant albedo. It effectively responds to environmental factors such as irradiance, temperature, and wind speed. A correction of the optical model with a variable albedo is considered. This new model better accounts for the environmental influence and significantly improves the simulation. It reaches errors lower than 5% for power and 2% for energy estimation.

The simplified model shows promising results for the simulation of the VBPV installation, but is constrained by the assumptions in the optical and thermal models. Future work should validate the proposed models across diverse configurations—varying tilt angles, climates/locations, and module technologies—to provide stronger evidence of robustness.

Beyond simple parametric sweeps, subsequent studies should either perform a systematic sensitivity/parameter–influence analysis and increase model fidelity by adopting a 1-D thermal formulation, thereby improving environmental representation and output accuracy.

An explicit benchmark is also required: the present, experimentally validated optical-electrical-0D thermal model should be compared against established optical–electrical-1D thermal frameworks for PV modules (e.g., the only software validated optical–electrical-1D thermal approach of Gu et al. [16]). It is expected that 1-D physics improves accuracy by resolving through-thickness thermal gradients and unsteady heat-storage effects under rapid irradiance and wind transients, whereas 0-D models retain advantages in computational efficiency and parameter parsimony for design-space screening and real-time applications. To this end, a rigorous 0-D vs 1-D thermal comparison on a shared experimental dataset, reporting standard accuracy metrics and computational-cost indicators, should be carried out.

CRediT authorship contribution statement

Emanuele Ogliari: Writing – review & editing, Writing – original draft, Validation, Supervision, Resources, Methodology, Investigation, Formal analysis, Conceptualization, Visualization. **Alberto Dolara:** Writing – review & editing, Visualization, Validation, Methodology, Investigation, Formal analysis, Conceptualization. **Domenico Mazzeo:** Writing – review & editing, Writing – original draft, Validation, Supervision, Software, Methodology, Data curation, Conceptualization, Formal analysis, Investigation, Visualization. **Luca Lazzari:** Writing – original draft, Software, Investigation, Data curation. **Sonia Leva:** Writing – review & editing, Visualization, Validation, Project administration, Funding acquisition, Formal analysis, Conceptualization.

Declaration of competing interest

The authors declare that they have no known competing financial interests or personal relationships that could have appeared to influence the work reported in this paper.

Acknowledgments

This study was partly conducted within the Agritech National Research Centre and received partial funding from the European Union Next-GenerationEU (PIANO NAZIONALE DI RIPRESA E RESILIENZA (PNRR)—MISSIONE 4 COMPONENTE 2, INVESTIMENTO 1.4—D.D. 1032 17/06/2022, CN00000022). This manuscript reflects only the authors' views and opinions; neither the European Union nor the European Commission can be considered responsible for them. All authors have contributed equally. This work was supported in part by the "Ministero dell'Istruzione, dell'Università e della Ricerca, Italy" (Italy) under the Grant PRIN2020–HOTSPHOT 2020LB9TBC.

Data availability

Data will be made available on request.

References

[1] Wang X, Kurdgelashvili L, Byrne J, Barnett A. The value of module efficiency in lowering the levelized cost of energy of photovoltaic systems. Renew Sustain Energy Rev 2011;15(9):4248–54. http://dx.doi.org/10.1016/j.rser.2011.07.125.

[2] Patel T, Khan M, Sun X, Alam M. A worldwide cost-based design and optimization of tilted bifacial solar farms. Appl Energy 2018;247:467–79. http://dx.doi.org/10.48550/arXiv.1812.07849.

[3] Yusufoglu U, Pletzer T, Koduvelikulathu L, Comparotto C, Kopecek R, Kurz H. Analysis of the annual performance of bifacial modules and optimization methods. IEEE J Photovoltaics 2015;5:320–8. http://dx.doi.org/10.1109/JPHOTOV.2014.2364406.

[4] Ramírez-Ledesma J, Almeida R, Martínez-Moreno F, Rossa C, Martín-Rueda J, Narvarte L, Pigueiras E. A simulation model of the irradiation and energy yield of large bifacial photovoltaic plants. Sol Energy 2020;206:522–38. http://dx.doi.org/10.1016/j.solener.2020.05.108.

[5] Sahu P, Roy J, Chakraborty C. Performance assessment of a bifacial PV system using a new energy estimation model. Sol Energy 2023;262:111818. http://dx.doi.org/10.1016/j.solener.2023.111818.

[6] Ernst M, Liu X, Asselineau C-A, Chen D, Huang C, Lennon A, Lennon A. Accurate modelling of the bifacial gain potential of rooftop solar photovoltaic systems. Energy Convers Manage 2024;300. http://dx.doi.org/10.1016/j.enconman.2023.117947.

[7] Ernst M, Asselineau C-A, Tillmann P, Jäger K, Becker C. Modelling bifacial irradiance – step-by-step comparison and validation of view factor and ray tracing models. Appl Energy 2024;369:123574. http://dx.doi.org/10.1016/j.apenergy.2024.123574.

[8] Singh JP, Aberle A, Walsh T. Electrical characterization method for bifacial photovoltaic modules. Sol Energy Mater Sol Cells 2014;127:136–42. http://dx.doi.org/10.1016/j.solmat.2014.04.017.

[9] International Electrical Commission. Photovoltaic devices – Part 1-2: Measurement of current-voltage characteristics of bifacial photovoltaic (PV) Devices. Standard IEC 60904-1-2:2024, IEC; 2024.

[10] Bouchakour S, Valencia D, Luna A, Roman E, Kouadri Boudjelthia EA, Rodríguez P. Modelling and simulation of bifacial PV production using monofacial electrical models. Energies 2021;14:4224. http://dx.doi.org/10.3390/en14144224.

[11] Mannino G, Tina G, Jiménez Castillo G, Cacciato M, Bizzarri F, Canino A. Nonlinear and multivariate regression models of current and voltage at maximum power point of bifacial photovoltaic strings. Sol Energy 2024;269:112357. http://dx.doi.org/10.1016/j.solener.2024.112357.

[12] Osama A, Tina GM, Gagliano A. Thermal models for mono/bifacial modules in ground/floating photovoltaic systems: A review. Renew Sustain Energy Rev 2025;216:115627. http://dx.doi.org/10.1016/j.rser.2025.115627.

[13] Tina GM, Osama A, Cazzaniga R, Cicu M, Hancock J, Howlin E, Rosa-Clot M, Rosa-Clot P. Pvsails: Harnessing innovation with vertical bifacial PV modules in floating photovoltaic systems. Prog Photovolt, Res Appl 2024;32(12):872–88. http://dx.doi.org/10.1002/pip.3841.

[14] Willockx B, Lavaert C, Cappelle J. Performance evaluation of vertical bifacial and single-axis tracked agrivoltaic systems on arable land. Renew Energy 2023;217:119181. http://dx.doi.org/10.1016/j.renene.2023.119181.

[15] Mazzeo D, Di Zio A, Pesenti C, Leva S. Optimizing agrivoltaic systems: A comprehensive analysis of design, crop productivity and energy performance in open-field configurations. Appl Energy 2025;390:125750. http://dx.doi.org/10.1016/j.apenergy.2025.125750.

[16] Gu W, Ma T, Li M, Shen L, Zhang Y. A coupled optical-electrical-thermal model of the bifacial photovoltaic module. Appl Energy 2020;258:114075. http://dx.doi.org/10.1016/j.apenergy.2019.114075.

[17] Mermoud A, Wittmer B. PVSYST user's manual. 2014, Switzerland.

[18] Blair N, DiOrio N, Freeman J, Gilman P, Janzou S, Neises T, Wagner M. System advisor model (SAM) general description (Version 2017.9. 5). Tech. rep., National Renewable Energy Laboratory (NREL), Golden, CO (United States); 2018.

[19] McAdams WH. Heat Transmission. 3, McGraw Hill; 1954.

[20] Solar radiation. In: Solar engineering of thermal processes. John Wiley & Sons, Ltd; 2013, p. 3–42. http://dx.doi.org/10.1002/9781118671603.ch1, arXiv:https://onlinelibrary.wiley.com/doi/pdf/10.1002/9781118671603.ch1.

[21] Hottel HC, Sarofim AF. Radiative transfer, McGraw-Hill book company, new york, 1967. 52 pages. AIChE J 1969;15(5).

[22] Klein SA, et al. TRNSYS 18: Transient System Simulation Tool. Madison, WI, USA: Solar Energy Laboratory, University of Wisconsin–Madison; 1975, http://sel.me.wisc.edu/trnsys, Accessed: 2025-12-28.

[23] Mazzeo D, Matera N, Bevilacqua P, Arcuri N, et al. Energy and economic analysis of solar photovoltaic plants located at the University of Calabria. Int J Heat Technol 2015;33(4):41–50.

[24] Perez R, Stewart R, Seals R, Guertin T. The development and verification of the Perez diffuse radiation model. 1988.

[25] Sahu PK, Batzelis EI, Chakraborty C, Roy J. Electrical modeling of bifacial PV modules. IEEE J Photovoltaics 2024. http://dx.doi.org/10.1109/JPHOTOV.2024.3501403.

[26] Dolara A, Mazzeo D, Cabrera-Tobar A, Ogliari E, Leva S. Fully integrated optical-electrical-thermal model of bifacial photovoltaic modules for energy yield assessment. Lect Notes Electr Eng 2025;1275 LNEE.

[27] Becerra VG, Valdivia-Lefort P, Barraza R, García JG. Electrical model analysis for bifacial PV modules using real performance data in laboratory. Energies 2024;17(23). http://dx.doi.org/10.3390/en17235868.

[28] Lu Y, Wang J, Liu P, Rafee R, Rashidi S, Li G. Experimental and numerical study of solar cell performance under different shading conditions. Sol Energy 2025;296. http://dx.doi.org/10.1016/j.solener.2025.113599.

[29] Janssen GJ, Van Aken BB, Carr AJ, Mewe AA. Outdoor performance of bifacial modules by measurements and modelling. 77, 2015, p. 364–73. http://dx.doi.org/10.1016/j.egypro.2015.07.051,

[30] Dolara A, Leva S, Manzolini G. Comparison of different physical models for PV power output prediction. Sol Energy 2015;119:83–99. http://dx.doi.org/10.1016/j.solener.2015.06.017.

[31] Ogliari E, Bolzoni A, Leva S, Mussetta M. Day-ahead PV power forecast by hybrid ANN compared to the five parameters model estimated by particle filter algorithm. In: Villa AE, Masulli P, Pons Rivero AJ, editors. Artificial neural networks and machine learning – ICANN 2016. Cham: Springer International Publishing; 2016, p. 291–8.

[32] Doucet A, de Freitas N, Gordon N. An introduction to sequential Monte Carlo methods. In: Doucet A, de Freitas N, Gordon N, editors. Sequential Monte Carlo methods in practice. New York, NY: Springer New York; 2001, p. 3–14. http://dx.doi.org/10.1007/978-1-4757-3437-9-1.

[33] Fébba DM, Rubinger RM, Oliveira AF, Bortoni EC. Impacts of temperature and irradiance on polycrystalline silicon solar cells parameters. Sol Energy 2018;174:628–39. http://dx.doi.org/10.1016/j.solener.2018.09.051.

[34] Ben Haj Rhouma MBH, Gastli A, Ben-Brahim L, Touati FA, Benammar MA. A simple method for extracting the parameters of the PV cell single-diode model. Renew Energy 2017;113:885–94. http://dx.doi.org/10.1016/j.renene.2017.06.064.

[35] Migliorini L, Molinaroli L, Simonetti R, Manzolini G. Development and experimental validation of a comprehensive thermoelectric dynamic model of photovoltaic modules. Sol Energy 2017;144:489–501. http://dx.doi.org/10.1016/j.solener.2017.01.045.

[36] Krauter SC. Solar Electric Power Generation: Photovoltaic Energy Systems. Springer; 2006.

[37] Swinbank WC. Long-wave radiation from clear skies. Q J R Meteorol Soc 1963;89(381):339–48. http://dx.doi.org/10.1002/qj.49708938105.

[38] SolarTech Lab - Politecnico di Milano. 2024, Available at: https://www.energia.polimi.it/laboratori/laboratorio-di-tecnologie-solari-stl/. Accessed on 2024-10-25.